Effects of Vacancy-Defected, Dopant and the Adsorption of Water upon Mn_2O_3 and Mn_3O_4 (001) Surfaces: A First-Principles Study

M. Mansouri*

Department of Physics, Mashhad Branch, Islamic Azad University, Mashhad 9187147578, Iran

(Received May 14, 2017; in final form November 8, 2017)

In this study, a first-principles study using the spin-polarized density functional theory approach within corrected functional was carried out to investigate the electronic features of manganese oxide surfaces under three situations of (a) cation vacancy, (b) intercalation of multi- and univalent ions, and (c) adsorption of a water molecule upon the surface as catalytic performance. The possibility of obtaining the significant absolute magnetic momentum phases from native defects in orthorhombic structures of Mn_2O_3 and Mn_3O_4 (001) surface is explored, whereas Mn vacancy provides a transition from the insulating phase into a metal-like nature and modifies the electronic transport. Moreover, bandgap engineering via impurity intercalation has been explored. Ca^{+2} and Al^{+3} intercalations have manifested substantial attributes and explain the experimental results as efficient conducting system and catalytic activity. Furthermore, the adsorption of one water molecule and the most stable configuration, adsorption energies and electronic properties were thoroughly discussed. Accordingly, it was explored that H_2O: Mn_2O_3 and Mn_3O_4 exhibit suitable parameters as efficient catalytic synthesis.

DOI: 10.12693/APhysPolA.133.1178

PACS/topics: manganese oxides, surface, vacancy, substitutional doping, adsorption

1. Introduction

Manganese oxides, Mn_xO_y, are technologically significant materials. Their electrochromic, spintronic, and the possibility of external ions intercalation and deintercalation give rise to diverse potential applications in electronic devices like rechargeable batteries, electrochemical super capacitors, sensors, and biological systems as detoxification of superoxide free radicals in organisms [1–5]. In particular, they are widely utilized as the desirable catalyst for oxygen reduction-evolution reactions and efficient photocatalytic water splitting system. As a consequence, their characteristic features have been explored thoroughly by X-ray spectra [6, 7]. Moreover, manganese oxides have been regarded as the most favorable materials for hydrogen photocatalytic production via water splitting due to their high stability, photocatalytic activity, non-toxicity, and low cost [8, 9]. Quite recently, considerable attention is paid to improve the catalytic performance via diverse systematic approaches and treatments, experimentally [10, 11].

Manganese (Mn) is a multivalent element; each valence state, therefore, makes characteristic stoichiometric oxide phase or phases. These oxides crystallize in different lattice structures and symmetry space groups. The commonest oxidation states of manganese are +2, +3, and +4, namely $Mn^{II}O$, $Mn_3^{II,III}O_4$, $Mn_2^{III}O_3$, and $Mn^{IV}O_2$ [12]. As a matter of fact, the bandgap of these oxides is too large (more than 2.5 eV) to absorb a remarkable portion of visible light. However, the optical sorption and reflectivity of these materials can be attuned by injection or extraction of electrons and ions, giving excellent control over and tenability of their functionalities [13, 14]. Bandgap engineering is the process of altering the gap of materials [15]. This is typically done to insulators by controlling the composition of alloys or constructing layered materials with alternating combinations. Impurity dopant via atomic adsorption-substitution technique supplies extensive and diverse possibilities for fine-tuning bandgap width.

In the present article, after a brief discussion about the pure bulk properties of multivalent manganese oxides, attention will be focused on the Mn_3O_4 and Mn_2O_3 surface reconstruction and detailed analysis of the survey data will be performed. Due to the distinctive catalytic features, their structural and electronic properties will be discussed and a link to the empirical findings will recall as a comparison. Next, the case of Mn cation vacancy-defect and substitutional doping by multi- and univalent ions is considered. Lastly, an initial investigation of the electronic structure of these surfaces will be simulated, when a water molecule is adsorbed on the bare surface to explore the catalytic performance.

2. Calculation method

All staggering calculations were carried out using the Quantum ESPRESSO package which is a plane wave basis set code [16]. The basis set is used to represent the valence orbitals of the system when its size is controlled by the kinetic-energy cutoff (E_{cut}). Therefore, an E_{cut} value of 30 Ry ($\approx$ 400 eV) is obtained by convergence

*corresponding author; e-mail: ma.mansoury@gmail.com

tests for the whole of the Mn_xO_y systems to permit comparison on an equal scale. The valence electrons were taken to be $2s^2 2p^4$ for O and $3d^5 4s^2$ for Mn. Due to the half-filled d-states of manganese atom, it is reported that electronic structure calculations using density functional theory (DFT) profoundly depend on the details of the exchange-correlation functional used [17]. Accordingly, generalized gradient approximation (GGA), and BLYP functional are used for electron exchange-correlation for whole systems in bulk phase [18, 19].

To achieve optimized settlement between computing time and accuracy, 8×8×8 grid including the Γ-point was chosen for the least difficult cases of MnO and MnO_2, whose unit cells contain only two and six atoms, respectively. For Mn_3O_4, with 28 atoms per unit cell, a 4×4×4 same mesh was applied, while for Mn_2O_3, with 80 atoms per unit cell, just the Γ-point was chosen. A structural model of the unit cells is shown in Fig. 1. All

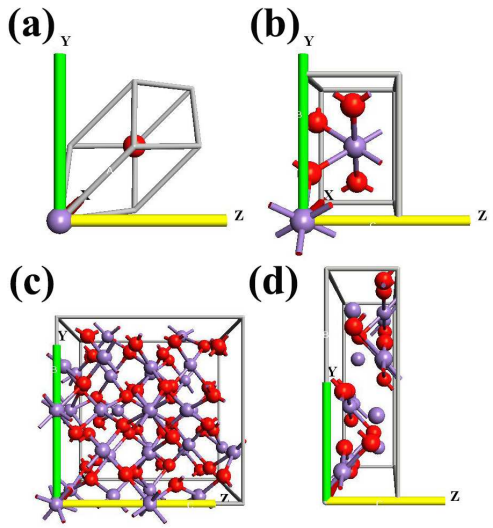

Fig. 1. The optimized primitive unit cells of (a) MnO, (b) MnO_2, (c) Mn_2O_3, and (d) Mn_3O_4. Blue and red spheres indicate Mn and O atoms, respectively.

k-point meshes were generated by the Monkhorst–Pack method [20]. Moreover, a Gaussian broadening with a width of 10^{-2} eV for smearing was used to guarantee the accuracy up to 10^{-3} Ry. Unit cell volumes and atomic positions have been relaxed to obtain geometrical optimization until the stress tensor, interatomic forces, and total energies were reduced to less than 10^{-3} (Ry/Å). A thorough and detailed discussion about the surface simulation is given in the appropriate subsection.

3. Results and discussion

3.1. Properties of bulk manganese oxides

Recently, the bulk characteristics of manganese oxides have been extensively investigated using a wide variety of methods. In this section, a summary report on the ground-state properties of manganese oxides will be delivered, while the main aim of this study is to simulate their surface. Table I lists major parameters of the oxides investigated. Calculated results in this work bear a close resemblance to what is previously obtained by other theoretical studies based on hybrid and other functional [17, 21]. In order to ensure the criteria which are performed, calculated volumes are compared to the experimental measurements via relative error, whereas an underestimate prediction of the volumes is obtained.

The magnetic properties and unusual magnetic orderings of multivalent manganese oxides have been studied experimentally. It is reported that MnO and Mn_2O_3 crystallize in the antiferromagnetic phase when Mn_3O_4 exhibits ferrimagnetic behavior and MnO_2 has a helically ordered moment [22, 23]. In this work, a spin-polarized calculation was performed and an absolute magnetic moment (M) in all Mn oxides is calculated (see Table I). Furthermore, from the total density of states (TDOS) and band structure, as illustrated in Fig. 2, the bandgap between valence band (VB) and conduction band (CB) is observed to be assessed and compared with earlier studies both experimentally and theoretically. BLYP functional predicts an insulated ground-state for all Mn oxides; when the calculated bandgaps are underestimated in comparison with the experimental measurements. One can notice that MnO, MnO_2, and Mn_2O_3 exhibit a direct band; meanwhile the top of VB and the bottom of CB locate in Γ-point. It is shown that Mn_3O_4 crystalline structure has two possible direct pass at Γ and M points with similar magnitude at the Brillouin zone. For Mn_2O_3, the highest state of the VB from Γ to other points also is fairly flat, indicating to a minute energy difference between these points, which might be the reason for reporting diverse points as VB maxima using different DFT approaches. Furthermore, VBs in Mn_2O_3 and Mn_3O_4 are comparatively flat in comparison with CBs, which shows a large effective mass for the holes. As shown in relevant DOSs, the sharp peaks along VBs near the Fermi level are consistent with the flat bands. CBs, on the other hand, indicate high dispersive feature along the symmetrical points which indicates a low effective mass of electrons. Such potential characteristics will lead to stunningly electronic behaviors. Moreover, it is demonstrated that VBs are mostly composed of O $2p$ and Mn $3d$ orbitals while the CBs are solely formed by the contribution of Mn $3d$ orbitals. This is fairly common among transition metal oxides as described abundantly [24].

3.2. Surface (001) reconstruction

In the succeeding sections, attention will be focused on the Mn_3O_4 and Mn_2O_3 surface reconstruction for the following reasons. Firstly, theoretical surface studies by a vast number of computational approaches on MnO and MnO_2 surfaces have been fully developed to investigate the structural, electronic, and magnetic properties of these materials in agreement with empirical evidences [31–33]. Secondly, recent experimental studies

recommend that Mn_3O_4 and Mn_2O_3 compounds due to the stabilization and concentration of the Mn^{+3}, exhibit distinctly catalytic performance [34, 35]. Therefore, a detailed presentation of the MnO and MnO_2 surface reconstruction is beyond the purposes of the present study and it will be described elsewhere. Thus, after a brief discussion of the computational methods used in the search of theoretically stable models, consideration will be focused on the electronic structure of Mn_3O_4 and Mn_2O_3 surfaces.

TABLE I

Lattice parameter, unit cell volume, and electronic bandgap for ground-state Mn oxides; the comparison with experimental volumes is given regarding the relative error. All values have been calculated per one Mn_xO_y formula unit in the solid phase to permit comparison on an equal scale.

System	Space group	Lattice parameter [Å]				Vol. [Å^3]	Bandgap [eV]			E_{tot} [keV]	M [μ_B]
			a	b	c	Error [%]	Exp.	PBE [17]	This work		
MnO	$Fm3m$	This work	4.312	4.312	4.312	20.040 (-8%)	3.6 [25]	3.8	2.26	3.284	4.86
		Exp. [26]	4.445	4.445	4.445	21.953					
MnO_2	$P4_2/mnm$	This work	4.341	4.341	2.784	52.459 (-5%)	1.3-2.2 [27]	1.5	1.74	3.721	3.15
		Exp. [26]	4.396	4.396	2.871	55.481					
Mn_2O_3	$Pcab$	This work	9.217	9.331	9.174	789.077 (-5%)	3.2 [28]	1.1	2.83	7.005	8.10
		Exp. [29]	9.416	9.423	9.405	834.451					
Mn_3O_4	$Pmab$	This work	9.126	9.711	3.116	276.146 (-2%)	2.3-2.5 [28]	2.4	1.82	5.876	7.29
		Exp. [30]	9.556	9.799	3.024	283.194					

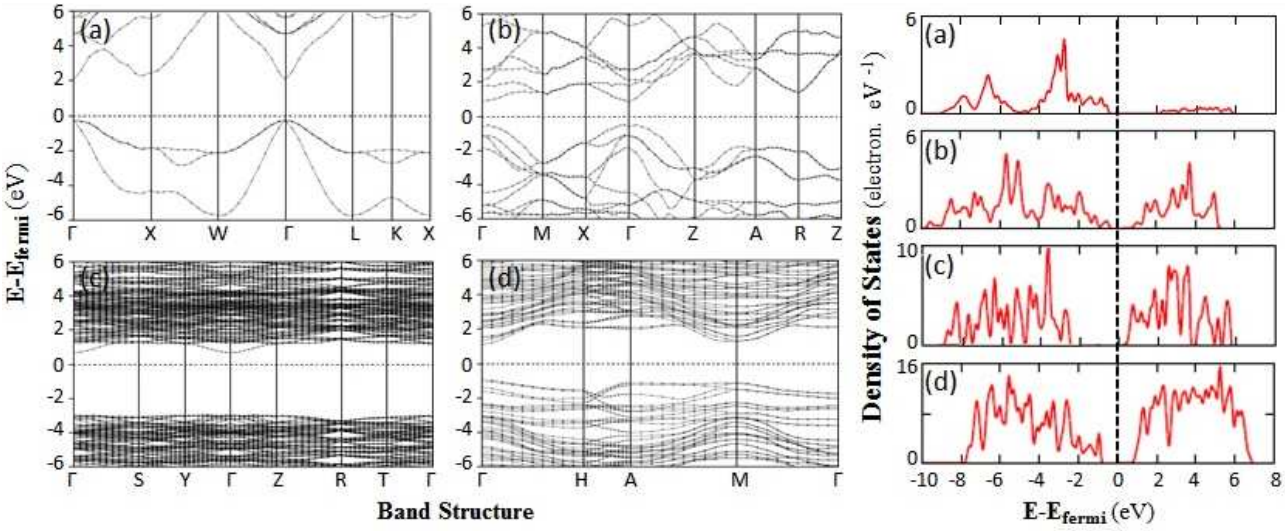

Fig. 2. Electronic band structure and TDOS by the standard BLYP functional for the ground state of (a) MnO, (b) MnO_2, (c) Mn_2O_3, and (d) Mn_3O_4. The high symmetry phases present direct Γ-point bandgap. All diagrams are aligned to have a common Fermi level, $E_{Fermi} = 0$

To investigate surfaces, the supercell approach is employed. In each case, to reduce the interaction of the close periodical image an orthorhombic unit supercell is considered with a vacuum gap placed upon it. The supercells of Mn_3O_4 and Mn_2O_3 consist of 28 and 80 atoms with respect to the bulk configuration, repeated periodically with vacuum gap of 18 Å ($c = 21.168$) and 38 Å ($c = 47.023$), respectively. In fact, the surface morphology has a prominent impact on surface energy. Therefore, three low-indexed (010), (001), and (100) surfaces were investigated in order to reconstruct the surface. In addition, there are two possible cleaved terminations for these orientations: either a surface completely covered with Mn (T_{Mn}) or a mixed Mn and O (T_{Mn-O}) when the former being the least stable one. Then, surfaces were represented by one exterior layer consisting of both Mn and O atoms with relaxation while interior layers had been fixed. The Brillouin zone k-point was carried out just in Γ-point. Finally, the strain and total energies per repeated slab have been computed and listed in Table II. It is (001) surface which is presented the lowest energies for both oxides. Thus, (001) surfaces with the termination of T_{Mn-O} are selected as a favorable configuration based on equilibrium morphology theory as well as predicted by previous theoretical calculations [36]. In fact, a recent experiment has provided evidence which

Mn_3O_4 can be cleaved to (001) oriented surfaces and its experimental growth has been achieved on Pd and MgO substrates under suitable preparatory conditions [37].

TABLE II

Total slab energy [keV] for the three low-indexed surfaces and different terminations.

Surface	010		001		100	
	T_{Mn}	T_{Mn-O}	T_{Mn}	T_{Mn-O}	T_{Mn}	T_{Mn-O}
Mn_2O_3	7391.4	7030.9	7313.4	7027.3	7386.3	7032.1
Mn_3O_4	6001.5	5869.3	5992.2	5868.7	5981.7	5874.2

Lately, Wang et al. have shown that DFT-GGA suffers from some systematic errors in evaluating the energy of oxidation reactions [38]. In these circumstances, DFT+U is an efficient remedy which is based on an addition to the DFT energy functional. For simulation involving the surface, calculations are performed by using both DFT and DFT+U approaches. The latter presents an electron–electron interaction as a correction in order to describe systems with localized *d*-state electrons which affect the anti- and ferromagnetic oxides. In the spirit of the Hubbard model Hamiltonian: as effective interaction parameter $U_{eff} = \bar{U} - \bar{J}$ was chosen where $\bar{U}$ and $\bar{J}$ are spherically averaged matrix elements of *on-site* Coulomb interactions in the localized *d*-state and *on-site* exchange parameter for Mn 3*d* within the approach of Dudarev et al. [39]. The equation that describes Hubbard correction energy (E_{Hub}) to the standard approximate DFT energy functional is as follows:

$$E_{\mathrm{Hub}} = \sum_{I,\sigma} \frac{1}{2} U^I_{eff} \mathrm{Tr}\left[n^{I\sigma}\left(1 - n^{I\sigma}\right)\right], \qquad (1)$$

Here I and σ are the atomic site index and the spin index (σ =1 or –1), respectively, and n is the occupation matrix. The values of 6.1 eV for Mn_3O_4 and 3.6 eV for Mn_2O_3 surfaces are obtained through this method.

As might be expected, DFT provides an unsatisfactory description when a metallic nature is assigned to both surfaces and the spin-polarized calculations have shown no magnetic momentum as a result of precise symmetry for the spin-up and down states in Mn_2O_3 surface. On the contrary, DFT+U approach has much better description. TDOS, presented in Fig. 3a, attributes half-metallic behavior to Mn_2O_3 surface when it acts like a metal in spin-up and an insulator on the opposite orientation. In spin-up, occupancy on the Fermi level is particularly considered where the Fermi energy (E_f) is located inside a widely uniform band.

For Mn_3O_4 the situations are roughly comparable for both approaches. Both DOS diagrams as shown in Fig. 3b depict a half-metal behavior, where the number of free states above E_f has significantly increased next to the insulating bulk's character. It results in higher conductivity as suggested by previous studies [40]. Moreover, DFT+U predicts that the bandgap between the highest occupied and lowest empty state of spin-up is become narrower. Interestingly, E_f is taken up by spin-down and illustrated metallic nature. Moreover, it is shown that occupied 3*d*-orbital states of Mn atoms play the major role around E_f while 2*p*-orbitals of oxygen predominantly have minor impact on entire VB. Free states above the Fermi states, on the other side, are mostly formed by unoccupied 3*d*-orbitals of Mn atoms. Further, total magnetization of 9.31 μB/cell is calculated as a direct result of these orbitals, which do not usually intervene in orbital hybridization and will lead to establishment of a magnetic localized area and magnetism demeanor.

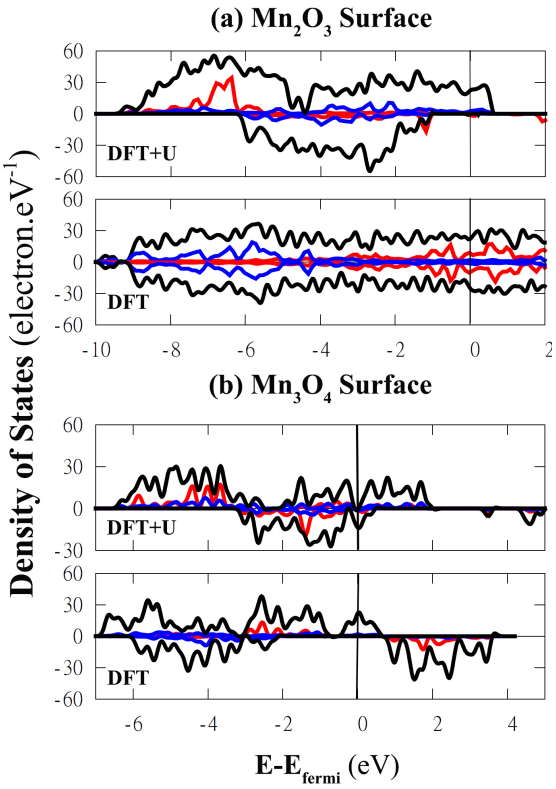

Fig. 3. Spin polarized TDOS for (a) Mn_2O_3 and (b) Mn_3O_4 thin films. Calculated results of DFT+U and DFT approaches are shown at the top and bottom for each case. Red and blue curves demonstrate projected DOS of Mn 3*d* and O 2*p* orbitals, respectively.

For a slab model, the surface energy (E_{sur}) is defined by following expression:

$$E_{sur} = (E_{slab} - nE_{bulk})/(2A) \qquad (2)$$

Here, E_{slab} is the total energy per repeated slab supercell and E_{bulk} stands for the total energy per unit cell in the bulk within DFT+U; n and A are number of unit cells and surface unit area, respectively. The factor 2 takes into account that the slabs are terminated by two identical surfaces. As a result, the values of E_{sur} were calculated to be +0.13 and –0.041 eV Å^{-2} for Mn_2O_3 and Mn_3O_4 surfaces. Accordingly, preparation of (001) Mn_2O_3 slab is comparatively more difficult and unstable than the Mn_3O_4.

3.3. Cation vacancy within (001) surface

An important characteristic method to investigate surface science in all materials is the presence of cation vacancy-defect. Vacancies in metal oxides can beget electron donors or acceptors. The spinel Mn_3O_4 is formed by both tetrahedral Mn^{+2} and octahedral Mn^{+3} cations in the intervening distorted cubic close-packed array of oxygen atoms [21]. The collinear antiferromagnetic structure of Mn_2O_3, on the other hand, is intrinsically composed by octahedral Mn^{+3} ions, when each O ion has four Mn neighbors [41]. For both Mn_2O_3 and Mn_3O_4 (001) surfaces, the orthorhombic unit supercell of V_{Mn} has been modeled by removing an octahedral Mn^{+3} at the topmost layer (T_{Mn-O}). Unit supercell of Mn_2O_3 consists of eight octahedral Mn^{+3} cations at topmost layer, while the Mn_3O_4 presented two Mn^{+2} and four Mn^{+3} cations allowing the representation as a ferrimagnetic model [42]. As a standard approach, convergence tests in total energy are performed by removing each of Mn^{+3} to determine the minimum total energy in defected supercells. Accordingly, specific cation with lowest energy was chosen to remove as Mn vacancy, i.e. $Mn_{1.94}O_3$ ($Mn_{31}O_{48}$) and $Mn_{2.75}O_4$($Mn_{11}O_{16}$). The calculations are carried out with the same structures used in the surface reconstruction, in order to make a direct comparison. Atomic positions are followed by relaxation where four surrounding oxygen atoms shift to the vacant position by around 0.3 Å. The total energy of relaxed V_{Mn} is calculated to use in the subsequent subsections.

Basically, cation vacancy in the majority of transition metal oxides induces magnetism. Due to this fact, defected structures of Mn_2O_3 and Mn_3O_4 with orthorhombic crystal symmetry have shown a significant magnetic momentum of 9.77 and 14.26 μB with a local magnetic moment on neighboring. Such profound magnetization in $Mn_{2.75}O_4$, which is 1.5 times higher than on clean (001) surface, stems from distortion in the octahedral site based on the Jahn–Teller effect, which transformed the electron density distribution. Moreover, it indicates a natural tendency for a transition to metal-like phase.

3.4. Cation substitution at the Mn site

The intercalation of multivalent cations, such as Ca^{+2} and Al^{+3} as well as univalent Li^+ and Na^+ into the surface is developing rapidly. There has been a great deal of research into the potential benefits of using this technique [43, 44]. Newly, some types of doped MnO_2 are used in commercial alkaline batteries due to their tunnel structure [45]. Consequently, computational modeling of such intercalations in the Mn_2O_3 and Mn_3O_4 (001) surfaces has been simulated. In this study, the dopant atom (Ð) is placed in the vacant position of Mn^{+3} ion through the external layer which is established in the previous subsection. Then, relaxation in variable cell and atomic position for a top atomic layer, which is composed by Mn and O and Ð, is carried out while lower layers were frozen. As a result, atomic positions are displaced by around four percent just for neighbors. Besides, lattice parameters have been altered mainly because the ionic radii of these dopants (Li^+: 0.9, Na^+: 1.16, Ca^{+2}: 1.14 and Al^{+3}: 0.67 Å) are quite different compared to Mn^{+3} (0.72 Å). Although, it is rightly expected that Al^{+3} ion is the most favorable dopant not only for identical oxidation state, but also for the closest ionic radius to Mn^{+3}.

DOS graphs are sketched in Fig. 4. A transition to metallic phase for all systems is exhibited. Moreover, projected DOSs show that orbital states of doped atoms are the main responsible of these marked changes. For both oxides, the number of states at Fermi level (ε) has increased significantly in comparison with the clean surface; the maximum number of ε is counted up for Ca and Na intercalation, which recommends applying them in conducting system or water-oxidizing catalyst [46]. Among all, Li and Na intercalations as n-type doping have provided the highest absolute magnetic moment and the spin splitting in both cases. It depicts powerful magnetic characteristic as result of the concentration of s-orbital which has striking impact on the magnetic attributes, magnetization quantity, and configuration of magnetic moments.

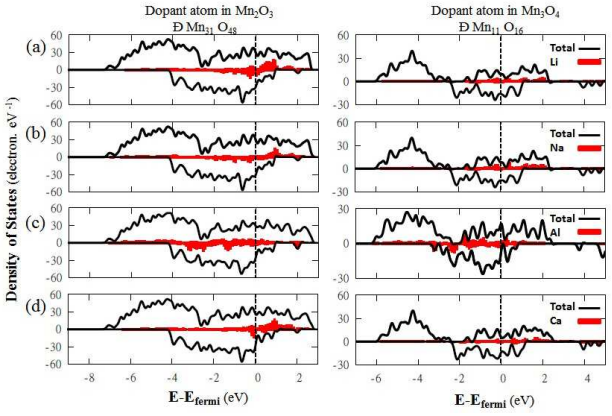

Fig. 4. TDOS diagrams for substitutional doping (a) Li, (b) Na, (c) Al, and (d) Ca cations at the Mn site for Mn_2O_3 (left) and Mn_3O_4 (right) surfaces within DFT+U. Shaded red curves demonstrate projected DOS of dopant s-orbital (for Li, Na, and Ca) and p-orbital (for Al).

Spin polarization (P) at the Fermi level as an influential parameter in the magnetism of half-metal systems is defined as:

$$P = (n^{\uparrow} - n^{\downarrow})/(n^{\uparrow} + n^{\downarrow}), \tag{3}$$

where $n^{\uparrow}$ and $n^{\downarrow}$ are the count of states at E_f in the spin-up and -down. In particular, $CaMn_{11}O_{16}$ as n-type doping shows highest spin polarization. The solubility or formation energy (E_{form}) of dopant atom in Mn_xO_y systems under ambient conditions can be calculated by the following equation:

$$E_{form} = E_{tot}(\text{Ð Mn}_{x-1}\text{O}_y) - E_{tot}(\text{Mn}_{x-1}\text{O}_y) - E_{tot}(\text{Ð}), \tag{4}$$

where, $E_{tot}(\text{ÐMn}_{x-1}\text{O}_y)$ and $E_{tot}(\text{Mn}_{x-1}\text{O}_y)$ represent the total energies of doped system and defected system

with one vacant position at the Mn site, respectively. E_{tot}(Ð) is the total energy of single dopant atom in the ground-state and optimized unit cell. Established values are summarized in Table III. A positive value ($\approx$ 1 eV) of E_{form} has been obtained by all Mn_2O_3 systems. This means that substitutional doping of these dopants in Mn_2O_3 is unlikely to form under thermodynamically equilibrium conditions. A similar situation is found for doped systems of Mn_3O_4 surface with the exception of Al $Mn_{11}O_{16}$ whose E_{form} turns out to be negative. This value is calculated to be –2.9 eV and illustrates energetically favorable mechanism. Therefore, the Al doping will occur easily. Various experimental studies have explored this possibility of doping by intercalating in the bulk Mn_3O_4 [47, 48]. Here it is demonstrated that the same is also possible at the top layer level within (001) surface.

TABLE III

Total states above the Fermi level (ε), magnetization, spin polarization and formation energy for substitutional doping at the Mn^{3+} site.

System	ε	M [μ_B]	P [%]	E_{form} [eV]
Li $Mn_{31}O_{48}$	13.63	9.62	1	1.55
Li $Mn_{11}O_{16}$	12.25	14.9	27	1.11
Na $Mn_{31}O_{48}$	13.75	9.61	2	1.50
Na $Mn_{11}O_{16}$	13.61	14.9	29	1.05
Al $Mn_{31}O_{48}$	13.71	9.57	8	0.88
Al $Mn_{11}O_{16}$	13.50	14.0	17	-2.90
Ca $Mn_{31}O_{48}$	13.83	9.55	6	1.49
Ca $Mn_{11}O_{16}$	13.75	14.7	42	1.10

3.5. Adsorption of water molecule upon Mn_2O_3 and Mn_3O_4 surface

To study the catalytic properties of Mn_2O_3 and Mn_3O_4 surfaces under reaction with a water molecule, an orthorhombic supercell including optimized vacuum gap was carried out when the center of mass of water molecule in the symmetric orientation is located upon the exterior layer within (001) surface. Note that neutral molecule is used in this study. To investigate the adsorption site of H_2O, the total energies of two possible sites are calculated for both Mn_2O_3 and Mn_3O_4: upon the topmost Mn atoms and upon topmost O atoms in terminated surface (T_{Mn-O}). Energetically, the adsorption upon one of O atoms is chosen as stable and likely site in each case. Upon reaching the adsorption site, crystalline lattices are optimized significantly. It is observed that atomic positions in the relaxed structures have shifted by smaller than 1% due to the saturation of the vacant sites. Despite, these small displacements led to a slight decrease in the interplanar distance between top and lower layers in the supercell without changing the surface structure.

The electronic structure of VB is profoundly involved in the catalytic mechanism. Therefore, DOS graphs within energy range of –7.0 to 8.0 eV have been computed (see Fig. 5). Besides, numerical DOS analyzes are

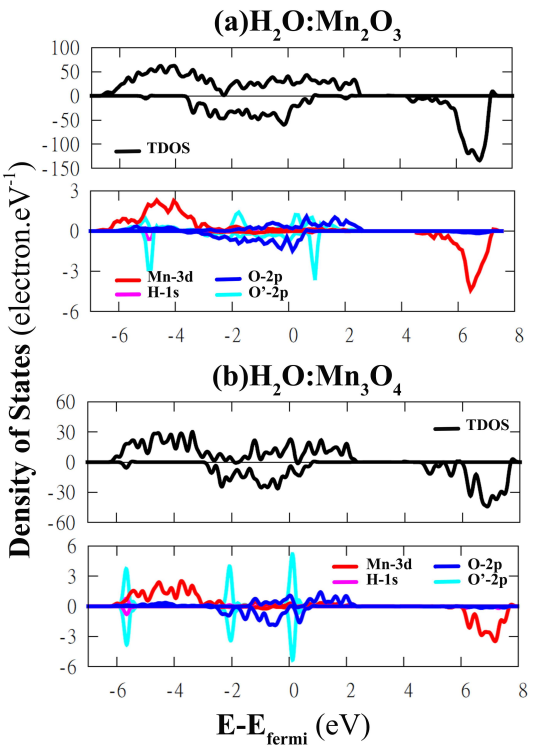

Fig. 5. Total and projected DOS diagrams of water adsorption upon (a) Mn_2O_3 and (b) Mn_3O_4 surfaces.

summarized in Table IV. Manganese atoms illustrate the major contribution in the early VB from –6 to –3 eV and entire CB that instinctively stems from 3*d*-orbitals, both occupied and unoccupied. On the contrary, the vast majority of states around Fermi level are formed by O 2*p*. Further, few thin peaks in VB and especially around Fermi edge are constructed by O*′* 2*p* state of water while negligible impact of hydrogen *s*-orbital is observed just on early VB. Overall, it can be seen that: (i) DOSs do not draw a distinction between valence and conduction bands and contribution of states has changed considerably. In particular, the bandgap, which had been previously predicted by (001) surface calculation, is disappeared. (ii) Adsorption on (001) surface exhibits metallic nature meanwhile spin-up and -down crossing Fermi level. Such dramatic transformation will effectively lead to marked improvement in mechanical strain, conductivity and ultimately phase transitions. (iii) for Mn_3O_4, the magnetization has decreased compared to clean surface, whereas the value of spin polarization around Fermi level presents an increase.

Adsorption energy (E_{ads}) as a significant indicator can be defined as

$$E_{ads} = E_{\mathrm{H_2O:Mn_xO_y}} - E_{\mathrm{Mn_xO_y(001)}} - E_{H_2O}, \qquad (5)$$

where $E_{H2O:MnxOy}$ refers to the total energy when a H_2O molecule is attached to the surface, E_{MnxOy} is the total energy of clean surface, and $E_{H2O}$is the energy of a single water molecule. The values were set in Table IV.

There are two notable points in these results. Firstly, both adsorption energies are found large and negative, indicating thermodynamical stability. It describes the adsorption possibility as the catalytic performance of these compounds which has been studied extensively in industrial and environmental applications. Secondly, water adsorption upon the surface of Mn_3O_4 is less energetically favorable than that of adsorption on the Mn_2O_3 surface as it has been successfully adopted in previous analyses of the manganese oxides [41].

TABLE IV

VB width, integral of DOS graph along VB, adsorption energy and equilibrium bond length of H and O atoms with nearest Mn and O atoms for the most stable configurations, E_{H2O} was calculated to be –34.44 Ry.

System	ΔVB [eV]	$\int VB\ [e^-]$ Per formula	E_{ads} [eV]	P [%]	M [μ_B]	Bond length [Å]		
						Mn-O′ O-O′	Mn-H′ O-H′	Mn-H″ O-H″
H_2O:Mn_2O_3	9.31	27.34	-1.36	8	10.11	3.45 3.04	2.90 1.42	2.84 1.59
H_2O:Mn_3O_4	8.94	39.03	-0.17	60	7.66	3.68 3.80	2.89 1.40	2.92 1.27

4. Conclusion

To conclude, the main objective of this study was set to analyze the structural, electronic, and magnetic properties of multivalent manganese oxides which were induced by various mechanisms of the vacancy-defected, absorption on the surface and identifying cation doping for fairly accurate determination of the electron–hole densities. It is firstly found that bulk states present an insulating ground-state for all Mn oxides with wide bandgap within BLYP functional. Moreover, surface (001) reconstruction has been considered for Mn_2O_3 and Mn_3O_4, when the most marked improvement in magnetism has been produced by a vacant position at Mn^{+3} site which prepared a significant absolute magnetic momentum in orthorhombic crystal symmetry. Cation substitution at the Mn^{+3} site has been also investigated as n-type doping via multi- and univalent ions and the formation energies are calculated. An interesting outcome of this investigation is that Al^{+3} doping will occur easily. Finally, adsorption of water molecule upon (001) surfaces is simulated. Due to the large and negative adsorption energies, Mn_2O_3 and Mn_3O_4 might be suitable for serving as a catalyst. Based on these arguments, results may be useful to exploit their considerable potential in industrial and environmental applications as well as electronic devices. Molecular dynamic and electronic properties of clusters will be probed in future investigations.

Acknowledgments

I am especially grateful to Dr. Annika Bande, Institute of Methods for Material Development at Helmholtz-Zentrum Berlin, for initial guidance and encouragement. I would like also to thank Dr. Tahereh Mahmoodi for stimulating discussions. Computational support was provided by Applied Biology Research Center, Department of Biology at the Islamic Azad University.

References

[1] M.C. Bernard, A. Hugot-Le Goff, B.V. Thi, S.C. de Torresi, *J. Electrochem. Soc.* **140**, 3065 (1993).

[2] K. Sato, H. Katayama-Yoshida, *Semicond. Sci. Technol.* **17**, 367 (2002).

[3] S. Jung, S.-J. An, G.-C. Yi, C. Jung, S.-I. Lee, S. Cho, *Appl. Phys. Lett.* **80**, 4561 (2002).

[4] A.E.S. Raj, C. Mallika, O. Sreedharan, K. Nagaraja, *Mater. Lett.* **53**, 316 (2002).

[5] G.S. Gund, D.P. Dubal, B.H. Patil, S.S. Shinde, C.D. Lokhande, *Electrochim. Acta* **92**, 205 (2013).

[6] F.H. Lima, M.L. Calegaro, E.A. Ticianelli, *J. Electroanal. Chem.* **590**, 152 (2006).

[7] Y. Gorlin, B. Lassalle-Kaiser, J.D. Benck, S. Gul, S.M. Webb, V.K. Yachandra, J. Yano, T.F. Jaramillo, *J. Am. Chem. Soc.* **135**, 8525 (2013).

[8] M.M. Najafpour, S.I. Allakhverdiev, *Int. J. Hydrogen Energy* **37**, 8753 (2012).

[9] R. Brimblecombe, A. Koo, G.C. Dismukes, G.F. Swiegers, L. Spiccia, *J. Am. Chem. Soc.* **132**, 2892 (2010).

[10] F. Jiao, H. Frei, *Chem. Commun.* **46**, 2920 (2010).

[11] S.L. Chang, A. Singh, R.K. Hocking, C. Dwyer, L. Spiccia, *J. Mater. Chem. A* **2**, 3730 (2014).

[12] A.F. Wells, *Structural Inorganic Chemistry*, Oxford University Press, 2012.

[13] C.G. Granqvist, *Handbook of Inorganic Electrochromic Materials*, Elsevier, 1995.

[14] P.M. Monk, R.J. Mortimer, D.R. Rosseinsky, *Electrochromism: Fundamentals and Applications*, Wiley, 2008.

[15] F. Capasso, *Science* **235**, 172 (1987).

[16] P. Giannozzi, S. Baroni, N. Bonini, M. Calandra, R. Car, C. Cavazzoni, D. Ceresoli, G.L. Chiarotti, M. Cococcioni, I. Dabo, A. Dal Corso, S. de Gironcoli, S. Fabris, G. Fratesi, R. Gebauer, U. Gerstmann, C. Gougoussis, A. Kokalj, M. Lazzeri, L. Martin-Samos, N. Marzari, F. Mauri, R. Mazzarello, S. Paolini, A. Pasquarello, L. Paulatto, C. Sbraccia, S. Scandolo, G. Sclauzero, A.P. Seitsonen, A. Smogunov, P. Umari, R.M. Wentzcovitch, *J. Phys. Condens. Matter* **21**, 395502 (2009).

[17] C. Franchini, R. Podloucky, J. Paier, M. Marsman, G. Kresse, *Phys. Rev. B* **75**, 195128 (2007).

[18] J.P. Perdew, K. Burke, M. Ernzerhof, *Phys. Rev. Lett.* **77**, 3865 (1996).

[19] B. Miehlich, A. Savin, H. Stoll, H. Preuss, *Chem. Phys. Lett.* **157**, 200 (1989).

[20] H.J. Monkhorst, J.D. Pack, *Phys. Rev. B* **13**, 5188 (1976).

[21] R. Ribeiro, S. de Lazaro, S. Pianaro, *J. Magn. Magn. Mater.* **391**, 166 (2015).

[22] M. Regulski, R. Przeniosło, I. Sosnowska, D. Hohlwein, R. Schneider, *J. Alloys Comp.* **362**, 236 (2004).

[23] A. Cheetham, D. Hope, *Phys. Rev. B* **27**, 6964 (1983).

[24] M. Mansouri, T. Mahmoodi, *Acta Phys. Pol. A* **129**, 8 (2016).

[25] N. Iskenderov, I. Drabkin, L. Emel'yanova, Y. Ksendzov, *Sov. Phys. Solid State* **10**, 2031 (1969).

[26] R. Wyckoff, *Crystal Structures*, Vol. 1, Interscience Publ., New York 1963.

[27] D.A. Tompsett, D.S. Middlemiss, M.S. Islam, *Phys. Rev. B* **86**, 205126 (2012).

[28] S. Gnanam, V. Rajendran, *J. Sol-Gel Sci. Technol.* **58**, 62 (2011).

[29] S. Geller, *Acta Crystallogr. B* **27**, 821 (1971).

[30] C.R. Ross, D.C. Rubie, E. Paris, *Am. Mineral.* **75**, 1249 (1990).

[31] H. Momida, T. Oguchi, *J. Phys. Soc. Jpn.* **72**, 588 (2003).

[32] G.A. Oxford, A.M. Chaka, *J. Phys. Chem. C* **115**, 16992 (2011).

[33] E. Cockayne, L. Li, *Chem. Phys. Lett.* **544**, 53 (2012).

[34] D.M. Robinson, Y.B. Go, M. Mui, G. Gardner, Z. Zhang, D. Mastrogiovanni, E. Garfunkel, J. Li, M. Greenblatt, G.C. Dismukes, *J. Am. Chem. Soc.* **135**, 3494 (2013).

[35] Y. Gorlin, C.-J. Chung, D. Nordlund, B.M. Clemens, T.F. Jaramillo, *ACS Catal.* **2**, 2687 (2012).

[36] V. Bayer, R. Podloucky, C. Franchini, F. Allegretti, B. Xu, G. Parteder, M.G. Ramsey, S. Surnev, F.P. Netzer, *Phys. Rev. B* **76**, 165428 (2007).

[37] L. Guo, H. Ko, H. Makino, Y. Chen, K. Inaba, T. Yao, *J. Cryst. Growth* **205**, 531 (1999).

[38] L. Wang, T. Maxisch, G. Ceder, *Phys. Rev. B* **73**, 195107 (2006).

[39] S. Dudarev, G. Botton, S. Savrasov, C. Humphreys, A. Sutton, *Phys. Rev. B* **57**, 1505 (1998).

[40] P. Tasker, *J. Phys. C Solid State Phys.* **12**, 4977 (1979).

[41] M. Khan, J. Xiao, F. Zhou, M. Yablonskikh, D.R. MacFarlane, L. Spiccia, E.F. Aziz, *ChemSusChem* **8**, 1980 (2015).

[42] A. Chartier, P. D'Arco, R. Dovesi, V.R. Saunders, *Phys. Rev. B* **60**, 14042 (1999).

[43] S.H. Lapidus, N.N. Rajput, X. Qu, K.W. Chapman, K.A. Persson, P.J. Chupas, *Phys. Chem. Chem. Phys.* **16**, 21941 (2014).

[44] T. Mahmoodi, M. Mansouri, *J. Korean Phys. Soc.* **69**, 1439 (2016).

[45] R.K. Guduru, J.C. Icaza, *Nanomaterials* **6**, 41 (2016).

[46] N. Birkner, S. Nayeri, B. Pashaei, M.M. Najafpour, W.H. Casey, A. Navrotsky, *Proc. Natl. Acad. Sci. USA* **110**, 8801 (2013).

[47] Y.-S. Lee, N. Kumada, M. Yoshio, *J. Power Sources* **96**, 376 (2001).

[48] A. Yuan, L. Tian, W. Xu, Y. Wang, *J. Power Sources* **195**, 5032 (2010).